

# DIG3D: Marrying Gaussian Splatting with Deformable Transformer for Single Image 3D Reconstruction

Jiamin Wu<sup>1,2\*</sup>, Kenkun Liu<sup>2,3</sup>, Han Gao<sup>2</sup>, Xiaoke Jiang<sup>2</sup>, Lei Zhang<sup>2</sup>

<sup>1</sup>Hong Kong University of Science and Technology

<sup>2</sup>International Digital Economy Academy (IDEA)

<sup>3</sup>The Chinese University of Hong Kong, Shenzhen

## Abstract

In this paper, we study the problem of 3D reconstruction from a single-view RGB image and propose a novel approach called DIG3D for 3D object reconstruction and novel view synthesis. Our method utilizes an encoder-decoder framework which generates 3D Gaussians in decoder with the guidance of depth-aware image features from encoder. In particular, we introduce the use of deformable transformer, allowing efficient and effective decoding through 3D reference point and multi-layer refinement adaptations. By harnessing the benefits of 3D Gaussians, our approach offers an efficient and accurate solution for 3D reconstruction from single-view images. We evaluate our method on the ShapeNet SRN dataset, getting PSNR of 24.21 and 24.98 in car and chair dataset, respectively. The result outperforming the recent method by around 2.25%, demonstrating the effectiveness of our method in achieving superior results.

## 1 Introduction

3D reconstruction from a single-view RGB image is a challenging ill-posed problem in computer vision [7, 6]. Neural Radiance Field (NeRF) based methods [41, 29] have made significant progress in this task by regressing volume density and view-dependent RGB color from spatial coordinates and viewing directions. Recent advancements have focused on tackling these challenges by employing NeRF-based networks trained solely on RGB data. The training process involves minimizing the image RGB loss between the ground truth image and the image rendered through volume rendering using sampled NeRF points [41, 12, 10, 20]. However, NeRF’s implicit representation introduces challenges in terms of computational inefficiency and reliance on sampling algorithms, which restricted their further applications.

To address these challenges, 3D Gaussian splatting [13] is employed in the 3D reconstruction task as a faster alternative to NeRF. Instead of representing

---

\*This work is done during an internship in the International Digital Economy Academy (IDEA).

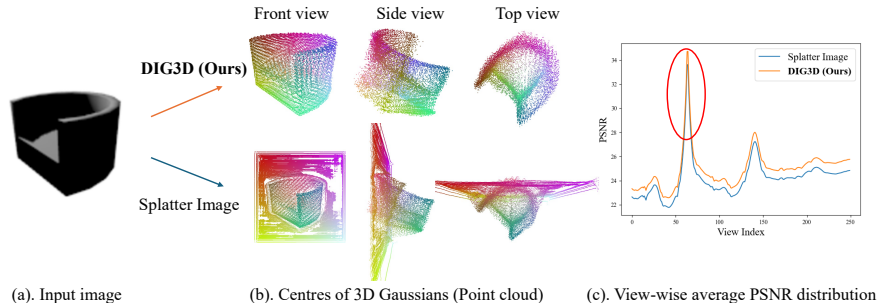


Figure 1: Comparison of our method and Splatter Image [37]. (a) Single view input image of a chair. (b) Centres of 3D Gaussians (Point cloud). We visualize the center of each Gaussian ellipsoid as a point cloud and present its main view, side view, and top view to approximate the generated object’s geometry. To ensure only significant points contributing to the object are counted, points with an opacity below 0.0003 were removed. More evaluation are in Figure 6 and Table 3. (c) View-wise average PSNR distribution on ShapeNet SRN [35] chair dataset for 250 views. The input view and with index 64 and neighbor views are highlighted within the red circle. Our method demonstrates improvement, particularly for views that are distant from the input view.

3D objects implicitly by a neural network, 3D Gaussian splatting utilizes explicit 3D Gaussian ellipsoids to represent objects and extends point-based rendering methods to obtain rendered views [38, 5]. With the help of explicit 3D representation and efficient point rendering, it provides a solution to avoiding the heavy sampling in NeRF but remains the advantage that only 2D supervision is required. By combining diffusion methods with Gaussian splatting rendering, [38, 5] achieve comparable 3D reconstruction results to previous state-of-the-art methods such as [24, 23], while significantly improving the generation speed. However, diffusion-based models still require more than one minute to obtain a 3D representation due to multiple denoising steps in the inference process.

By contrast, non-generation-based models only require a single forward pass during inference, making them extremely fast. For instance, Splatter Image [37] simply uses UNet [34, 36] on the input image and obtains the parameters of 3D Gaussians for each pixel [37]. The approach yields comparable results to previous single image 3D reconstruction baselines on the ShapeNet SRN benchmark [35], but achieves a significantly high speed of 38 FPS from a image

to a 3D object and 588 FPS for rendering. Although [37] makes a significant attempt at utilizing 3D Gaussian splatting in the single view 3D reconstruction task, the method still has some limitations.

As illustrated in Figure 1(c), the Splatter Image method achieves good Peak Signal-to-Noise Ratio (PSNR) for views close to the input view, but performs poorly for views that are far from the input view. One possible explanation for this behavior is that the method attempts to align each 3D Gaussian with every pixel of the input view, resulting in a bias towards views far from the input view. Moreover, this per-pixel regression approach leads to a concentration of a majority of the 3D Gaussians in a single plane, as depicted in Figure 1(b). These background points contribute marginally to the 3D object, resulting in incorrect geometry and wasteful rendering time. The incorrect geometry generated by Splatter Image can be attributed to obtaining 3D Gaussians through UNet with convolution, which introduces unwanted grid structures aligned to each pixel of the input image. Examining the three views in Figure 1(b), it is evident that the object’s geometry is attempting to match the pixels of the input view, resulting in obvious inaccuracies and a significant waste of 3D Gaussians. Moreover, the wrong geometry also limits the feasibility of applications such as converting 3D Gaussian distributions into point cloud representations or surface reconstruction [40, 28].

To address the limitations of per-pixel regression, we propose a novel approach, named *DIG3D*, which marries gaussian splatting with deformable transformer for single image 3D object reconstructing. In contrast to the local relationships captured by UNet, we leverage a transformer-based model that allows all pixels to contribute to the 3D Gaussian reconstruction. Transformer models, such as DETR (Detection Transformer) [3, 46] and its variants [46, 25, 33, 27, 14, 15, 17], have demonstrated remarkable performance in tasks involving position and property extraction from image features, including object detection and point tracing. Our task involves regressing the position and properties of 3D Gaussian ellipsoids, which shares similarities with DETR and its follow-ups, as they decode the position and size of bounding boxes from image features. To implement our approach, we initially employ a similar encoder structure as presented in [37] to obtain pixel-aligned features. We supervise this encoder with the input view to ensure that the extracted features facilitate accurate rendering of the input view. Additionally, we utilize a pretrained DINOv2 [31] model to extract depth-aware features, which helps resolve depth ambiguity in single-view images. We then design a hierarchical feature fusion block to fuse these two types of features. Next, we adapt the decoder of DETR to our 3D reconstruction task, where our objective is to decode the position and properties of 3D Gaussians. Specifically, we treat the 3D Gaussians as queries and iteratively update them with guidance from the image features. As demonstrated in Figure 1(c), our method outperforms [37], particularly for views that are far from the input view. Notably, our approach achieves a significantly improved 3D geometry reconstruction as shown in Figure 1(b), yielding correct geometries in most cases.

While the deformable attention mechanism in DETR offers a simple yet effective approach for decoding 3D Gaussians from input images, there is a challenge that needs to be addressed. In the detection task in DETR, the regression target is a 2D bounding box, which is not directly applicable to efficiently utilize the 3D nature of Gaussians. To overcome this challenge, we make two key adaptations to the DETR framework for handling 3D Gaussians. Firstly, we project the center of each 3D Gaussian onto the image plane, treating it as a reference point. This projection is crucial for selecting the most relevant features for the corresponding anchors. Secondly, we update the parameters in the multi-layer refinement process for 3D Gaussians using specific operations. For the rotation parameter, we employ multiplication to update its value, allowing for more accurate representation of the rotational aspect of the Gaussians. For the other parameters, such as position and size, we use addition to update their values. By incorporating these adaptations into the DETR framework, we can address the challenges posed by working with 3D Gaussians, allowing for more efficient and accurate reconstruction of the object geometry.

Our contributions can be summarized as follows:

- We introduce DIG3D, a straightforward and efficient approach for 3D reconstruction and novel view synthesis from a single RGB image.
- We present a novel encoder-decoder framework that regards 3D Gaussians as queries with depth-aware image features as guidance. This structure solves the conflict between novel views and input view pixel alignment in [37].
- We adapt deformable transformer utilized in 2D detection to 3D reconstruction task. We develop a 3D reference point projection technique on the image feature map and apply multilayer refinement on 3D Gaussian parameters.
- We conduct experiments on ShapeNet SRN benchmark [35] to demonstrate the effectiveness of our method.

## 2 Related Work

**3D Representations** Implicit functions such as Neural Radiance Field (NeRF) have found wide application in 3D reconstruction tasks [11, 29, 44, 39, 1, 32, 41, 2]. By leveraging rendering methods, the implicitly reconstructed objects can be rendered in specified views and the optimization only requires 2D supervision. NeRF represents a scene as a 5D function that outputs the radiance emitted in each direction at each point. The color of each pixel in the image can be rendered by integrating the points along the ray that passes through the pixel. NeRF enables high-fidelity rendering, making 3D tasks feasible with only 2D supervision. However, since all NeRF parameters are implicitly represented,

optimizing NeRF can be time-consuming. Despite efforts made to accelerate NeRF [8, 9, 19, 30, 18], the implicit representation remains slow and heavily relies on the quality of sampling algorithms.

Recently, 3D Gaussian splatting [13] has introduced a new approach for representing objects in 3D. Compared to NeRF, it extends the point-based rendering method and can be easily applied as a differentiable rendering method for 3D reconstruction tasks with only 2D supervision. Furthermore, 3D Gaussian splatting explicitly represents 3D objects as 3D Gaussian ellipsoids. This eliminates the need for sampling methods and significantly speeds up the optimization process without performance degradation.

**3D Reconstruction from Single-view Image** Due to the good accessibility of single-view images, there is also a stream of methods [42, 20, 37] exploring reconstructing objects from only a single-view image. [42] adapt the original NeRF from a per-scene optimization manner to a feed-forward manner, enabling the learning of object priors with large-scale data for training. As it utilizes the NeRF representation and volume rendering, the whole pipeline is still time-consuming. After 3D Gaussian splatting [13] was proposed, [37] introduce a fast approach for 3D reconstruction, achieving real-time rendering. However, their per-pixel regression design often leads to wrong object geometry and does harm to the novel view synthesis.

**Deformable Transformer** The Detection Transformer has gained significant popularity in detection tasks [3]. This architecture employs a transformer-based encoder-decoder framework, where the encoder captures global contextual information using self-attention mechanisms, and the decoder generates a sequence of object queries. These queries are then utilized to regress the position, width, and height of bounding boxes, similar to our task of regressing the position and properties of 3D Gaussians. Subsequent works, such as Deformable DETR [46], introduced deformable attention mechanisms to handle object deformations, while Cascade DETR employed a cascaded architecture for progressive refinement. Furthermore, [26] extended the structure to open-set detection by incorporating text embeddings, and [17] applied it to point tracing in video tasks. These follow-up works have expanded the applications of deformable attention beyond detection, showcasing its versatility in various computer vision domains.

### 3 Methods

In this section, we introduce our proposed DIG3D for 3D reconstruction from a single-view image. We begin by providing the necessary preliminaries for 3D Gaussian Splatting, as detailed in Section 3.1. Next, we introduce the formulation of the 3D reconstruction and novel view synthesis tasks using 3D Gaussian splatting in Section 3.2. In Section 3.3, we describe how we extract depth-aware image features in the encoder and iteratively update the pixel-free

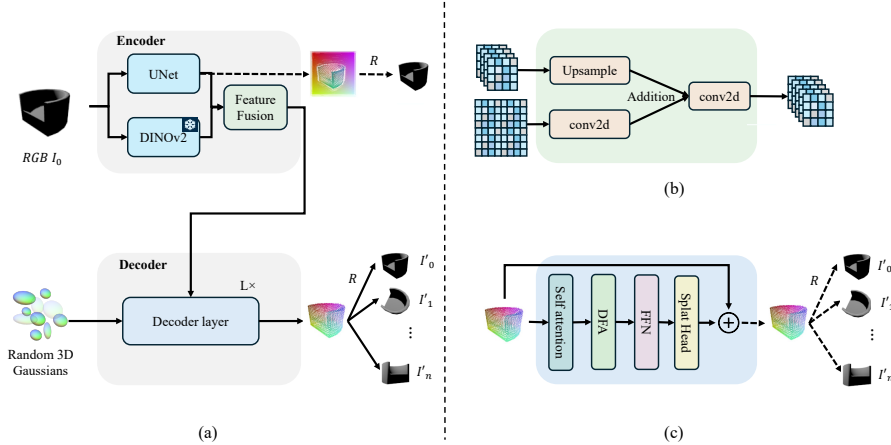


Figure 2: (a) Overview of DIG3D.  $\dashrightarrow$ : steps not utilized in inference. (b) Detailed structure for feature fusion in the encoder. (c) Detailed structure for one decoder layer. Queries are updated at each layer and serve as input for the next layer, while the reference points are updated based on the new centers of the Gaussians and projected onto the image feature plane. DFA: deformable cross attention layer; FFN: Feed Forward Network;  $\oplus$ : updation of 3D Gaussian.

3D Gaussians within the deformable transformer. Next, in Section 3.4, we show the adaption of our 3D Gaussians to deformable transformer. Finally, we discuss the training objective in Section 3.5.

### 3.1 Preliminaries of 3D Gaussian Splatting

We represent a 3D object using 3D Gaussian ellipsoids, characterized by their geometric and appearance parameters. The position and shape of an ellipsoid are determined by the mean vector  $\mu$  and the covariance matrix  $\Sigma$  of its corresponding 3D Gaussian distribution [47, 13]. Directly optimizing the covariance matrix can result in a non-positive semi-definite matrix [4]. Therefore, the covariance matrix can be optimized through a combination of rotation and scaling for each ellipsoid. This is achieved by expressing the covariance matrix as  $\Sigma = \mathbf{R}\mathbf{S}\mathbf{S}^T\mathbf{R}^T$ , where  $\mathbf{R}$  represents the rotation and  $\mathbf{S}$  contains the scales in three directions. The rotation is typically parameterized using quaternions, providing an efficient and effective way to represent the orientation of the ellipsoid.

In addition to position and shape, the 3D Gaussian is also parameterized by its opacity  $\sigma$ , which represents the likelihood of a light ray being blocked by the ellipsoid [29, 13]. When multiple 3D Gaussians lie along the same light ray, the final color of a pixel is calculated using  $\alpha$ -blending [29, 13] as shown below. In the context of 3D Gaussian splatting, which can be viewed as an extension of point-based rendering methods [13, 4], the color of a pixel  $\mathbf{p}$  on the image plane

can be rendered using point-based rendering techniques. The color  $C(\mathbf{p})$  at pixel  $\mathbf{p}$  can be expressed using the following equation:

$$C(\mathbf{p}) = \sum_{n \in N} c_n \alpha_n \prod_{j=1}^{n-1} (1 - \alpha_j), \quad (1)$$

$$\alpha_n = \sigma_n e^{\frac{1}{2}(\mathbf{p} - \mu_n)^T \Sigma_n^{-1} (\mathbf{p} - \mu_n)} \quad (2)$$

where  $N$  denotes the number of 3D Gaussians utilized to represent the 3D object.  $c_n, \sigma_n, \mu_n, \Sigma_n$  denotes the color, opacity, center, and covariance matrix of the  $n$ -th Gaussian.

When it comes to color representation in the Gaussian Splatting, using a simple RGB value is insufficient due to the fact that a 3D Gaussian ellipsoid represents more than just a single point. Instead, Spherical Harmonics (SH) [13] are employed to represent the view-dependent appearance of each ellipsoid. This approach allows for a more accurate and comprehensive representation of the color information associated with each 3D Gaussian ellipsoid.

## 3.2 Problem Formulation

We formulate the problem of single view 3D reconstruction as learning a mapping from single view images to 3D Gaussian parameters. Specifically, given a set of multi-view RGB images denoted as  $\mathcal{D} = \{I_{oj}, \pi_{oj} \mid o = 1, \dots, O; j = 1, \dots, J\}$ , where  $I_{oj} \in \mathbb{R}^{H \times W \times 3}$  represents the  $j$ -th image of the object  $o$  with dimensions  $H$  and  $W$ , and  $\pi_{oj}$  represents the camera pose for image  $I_{oj}$ , we aim to learn a mapping  $\mathcal{G}_\Phi$  that maps a given input image  $I_{oj}$  to a 3D object represented by  $N$  3D Gaussians  $\{G_n \mid n = 1, \dots, N\}$ . In other words, we want to obtain  $\theta_o = \mathcal{G}_\Phi(I_{oj})$ , where  $\theta_o = (\mu_n, \sigma_n, S_n, R_n, SH_n), n = 1, \dots, N$ . Each 3D Gaussian consists of parameters including the center  $\mu$ , opacity  $\sigma$ , covariance matrix  $\Sigma$  and spherical harmonic coefficients  $SH$ . Notably, instead of directly regressing the 3D coordinates of the center  $\mu$ , we regress the depth  $d$  and offset values  $(\Delta_x, \Delta_y, \Delta_z)$ . This choice simplifies the regression process and aids convergence (refer to Section 3.4 for more details). The Gaussian shape parameter  $\Sigma$  can be regressed using the scale  $S$  and rotation  $R$ . Subsequently, given the camera parameters  $\pi_{oj'}$ , we can render the  $j'$ -th novel view  $I_{oj'_{pred}} = \mathcal{R}(\mathcal{G}_2^l(I_{oj}), \pi_{oj'})$  and supervise it with the ground-truth  $I_{oj'}$ . For simplicity, we focus on outlining the training and inference procedure for a single image, omitting the subscript for subsequent sections.

## 3.3 DIG3D Framework

**Deformable 3D Gaussian Encoder** Reconstructing 3D objects from a single view is a highly ill-posed problem due to the depth ambiguity. Therefore, to relief

this issue, we design a depth-aware image encoder to extract both pixel-aligned features and depth-aware features from the input image, as shown in Figure 2(a).

We employ a UNet [34] architecture for extracting pixel-aligned features, following a similar approach to [37]. UNet offers a simple yet effective method for pixel-wise feature extraction. To effectively leverage the per-pixel correspondence provided by UNet in the input view and avoid conflicts in the position of novel view pixels, we introduce a loss on the reconstructed input view.

While we have obtained pixel-aligned image features, it is essential that these features also incorporate depth information to guide the 3D reconstruction process effectively. To address this, we utilize DINOv2, a model pretrained on the depth prediction task. DINOv2 inherently contains depth information due to its training on depth-related tasks. Hence, we leverage DINOv2 to acquire depth-aware image features. By incorporating depth information into the image features, we enhance the accuracy and reliability of our 3D reconstruction framework.

In order to harness the advantages offered by both the pretrained DINOv2 feature, which excels in 2D tasks and depth estimation, and the high-resolution UNet image feature, we introduce a feature fusion block as shown in Figure 2(b). Since the DINOv2 feature has a lower resolution compared to the UNet feature, we employ the concept of Feature Pyramid Networks (FPN) [21] to upsample the DINOv2 feature. After upsampling, we add the DINOv2 feature to the UNet feature followed with a convolution layer. This aggregated feature is then further processed using another convolution layer.

To reduce computational costs, the resulting feature with the original resolution is downsampled using a 2D convolution network with a large stride and kernel size. This downsampled feature serves as the feature map for deformable attention in the transformer decoder layers. This approach allows for efficient utilization of both the high-resolution UNet features and the informative pretrained DINOv2 features within the DIG3D method.

**Deformable 3D Gaussian Decoder** In the decoder phase, we initiate by randomizing  $N$  3D Gaussians as queries and strive to learn their parameters by leveraging the image features obtained from the encoder. Drawing inspiration from works such as [3, 43, 46], we integrate multiplayer refinement into our approach, computing the loss at the end of each layer. Additionally, we introduce a 3D reference point design, which enables us to adapt the 3D queries to the 2D deformable attention mechanism. By incorporating these techniques, we enhance the refinement process and improve the accuracy of our 3D reconstruction framework.

As depicted in Figure 2, we initialize  $N$  Gaussians and update them layer by layer in the transformer decoder. Within each layer, the 3D Gaussians undergo a self-attention operation to facilitate information exchange among all ellipsoids. Subsequently, they are utilized as queries to compute cross-attention with the image features via the Deformable Attention (DFA) mechanism [43, 46, 26, 16]. Ultimately, the queries are processed through a splat head to obtain the  $N \times K$  parameters for all the 3D Gaussians, where  $K$  denotes the number of Gaussian parameters for each Gaussian.

To be more precise, we represent the queries as  $\mathbf{q} \in \mathbb{R}^{N \times C}$ , where  $N$  denotes the number of 3D Gaussians used to represent an object, and  $C$  signifies the hidden dimension. The corresponding increments of 3D Gaussians  $\Delta G \in \mathbb{R}^{N \times K}$ , are computed by applying the splat head  $\mathcal{S}$  to the queries, as shown in Equation 3. The splat head is a convolution network that transforms the hidden dimension  $C$  into the output dimension  $K$ .

$$\Delta G = \mathcal{S}(\mathbf{q}) \quad (3)$$

In each layer, given a set of initialized queries  $\mathbf{q}$ , they undergo a self-attention operation to obtain updated queries. These updated queries are then utilized to compute the deformable cross-attention in conjunction with reference points and the fused image feature  $\mathbf{F}$ . Finally, the queries pass through a feed-forward network to complete one layer. Let  $l \in 1, 2, \dots, L$  denote the  $l$ -th layer of the decoder. The process of query updating in each layer can be described by Equation 4. Here, SelfAttn, DFA, and FFN represent the self-attention, deformable cross-attention, and feed-forward network, respectively.

$$\mathbf{q}^{l+1} = \text{FFN}(\text{DFA}(\text{SelfAttn}(\mathbf{q}^l), P^l, \mathbf{F})) \quad (4)$$

Here,  $P^l$  denotes the reference points at layer  $l$  and is obtained as follows. In each deformable cross-attention layer, we treat each 3D Gaussian ellipsoid as a 3D anchor and project its center onto the image feature plane, as depicted in Figure 3(b). By utilizing the pinhole camera model, the projection of the 3D points in camera coordinates can be described as  $P^l = C_{\text{intrinsic}} \mu^l / d$ , where  $C_{\text{intrinsic}}$  represents the camera’s intrinsic parameters.

### 3.4 Marrying 3D Gaussian to Deformable Decoder

**Multi-Layer Refinement** Taking inspiration from [43], we employ a multi-layer refinement strategy to enhance the decoding process and facilitate iterative improvement. This strategy involves updating the 3D Gaussians layer by layer. Initially, we obtain the initialized 3D Gaussians and proceed to train a parameter increment for each layer. We then update the 3D Gaussian parameters in a sequential manner, rendering and supervising them at each layer. This refinement process is denoted as  $\Delta G = \mathcal{S}_l(\mathbf{q}^l)$ , where  $\mathcal{S}_l$  represents the splat head of the  $l$ -th layer. To update the 3D Gaussian parameters from Gaussians  $G$  in the

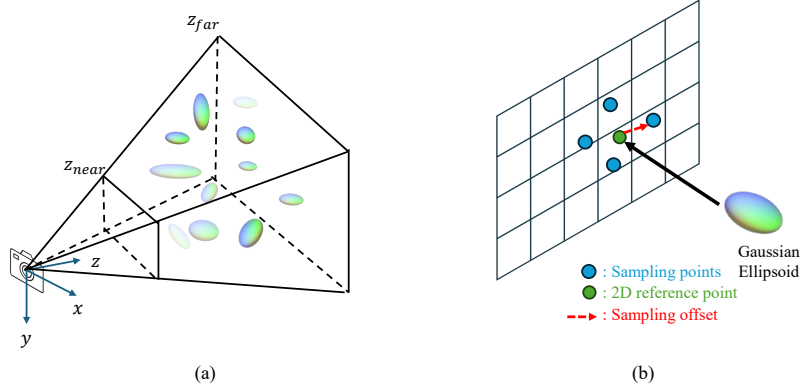


Figure 3: (a). We locate the centers of the 3D Gaussians within the visual cone, where  $z_{near}$  and  $z_{far}$  indicate the near and far clipping planes. The 3D object lies within the visual cone and falls within the desired depth range. (b). 3D Gaussian ellipsoid centers are projected onto the image feature maps, resulting in corresponding green points. By training sampling offsets from the green points to red sampling points, attention is performed using the features at the sampling points and queries.

previous layer, we apply the following change:  $G = G \oplus \Delta G$ . Here,  $\oplus$  denotes the update operation of  $G$  by  $\Delta G$ , involving multiplication for rotation and addition for other parameters.

Moreover, we compute the refined version of the reference points and utilize these updated reference points for deformable attention in the subsequent layer. By incorporating this strategy, we ensure that each layer contributes positively to refining the Gaussian representations.

Empirically, we find that directly regressing the center of 3D Gaussians can lead to convergence difficulties during training. To address this issue, our approach locates the 3D Gaussians within a visual cone, as illustrated in Figure 3(a). The center coordinates of the Gaussians. The center coordinates  $x, y, z$  are parameterized by the depth  $d$  and offset values  $(\Delta_x, \Delta_y, \Delta_z)$ . The depth  $d$  represents the length of a ray originating from the camera center. Then, the center coordinates  $\mu$  of a 3D Gaussian can be acquired with the below equation,

$$\mu = \begin{bmatrix} x \\ y \\ z \end{bmatrix} = \begin{bmatrix} u_1 d + \Delta_x \\ u_2 d + \Delta_y \\ d + \Delta_z \end{bmatrix} \quad (5)$$

Here  $d$  denotes the distance between Gaussian center and the normalized plane. The center of Gaussians can be derived by Equation 5. This design

simplifies the process of center regression in comparison to directly regressing the 3D Gaussian center coordinates. Similar to [37], we utilize 24 parameters to represent each 3D Gaussian ellipsoid. These parameters are distributed as follows: 4 parameters for  $\mu$  (1 for depth and 3 for position offset), 7 parameters for  $\Sigma$  (3 for scale  $\mathbf{S}$  and 4 for rotation  $\mathbf{R}$ ), 1 parameter for opacity  $\sigma$ , and 12 parameters for appearance  $SH$ .

**3D Reference Point** Although we have developed a fairly comprehensive framework for 3D reconstruction from a single RGB image, there remains a challenge regarding deformable attention. Deformable attention employs reference points and trains sampling offsets on image features to select sampling points for calculating cross-attention. This method efficiently performs cross-attention by selecting specific features in the image. In detection problems, the reference point is typically the center of the bounding box, and all operations are performed in the 2D image domain.

However, our situation differs in that we lack the bounding box center, and our queries are in 3D. To address this issue, we have devised a 3D reference point strategy. This strategy involves projecting the center of a 3D Gaussian onto the image features and considering it as the reference point, as depicted in Figure 3(b). Subsequently, we train sampling offsets  $\Delta S^l = \text{MLP}^S(\mathbf{q}^l)$  to determine the sampling points on the image features. These sampling points are crucial for calculating attention in conjunction with the queries.

To be more precise, the attention scores are computed using a Multilayer Perceptron (MLP) applied to the queries, while the values are obtained by bilinearly projecting the image feature at the sampling points. The update of queries from  $\mathbf{q}^l$  to  $\mathbf{q}^{l+1}$  through deformable cross-attention can be described by Equation 6.

$$\mathbf{q}^{l+1} = \sum_{p=1}^{N_P} A_p \text{Bilinear}(\mathbf{F}_l, P^l + \Delta S^l), A_p = \text{MLP}^A(\mathbf{q}^l) \quad (6)$$

In this equation,  $N_P$  represents the number of sampling points  $P$ , and  $\text{MLP}^A$  corresponds to the learnable MLP responsible for generating the attention weights.

### 3.5 Training objective

Given a RGB image  $I$  as input and the viewpoint change  $\pi$  between the source and target cameras, we compute the discrepancy between the ground truth image  $I_{gt}$  and the rendered views from encoder, as well as at each output layer of decoder. The overall loss function can be defined as Equation 7.

$$\mathcal{L} = \frac{1}{|\mathcal{D}|} \sum_{(I, I_{gt}, \pi) \in \mathcal{D}} (\|I - \mathcal{R}(\mathcal{G}_E(I), \pi)\|^2 + \sum_{l=1}^L \|I_{gt} - \mathcal{R}(\mathcal{G}_D^l(I), \pi)\|^2) \quad (7)$$

Here,  $\mathcal{R}$  represents the Gaussian splatting rendering operation using  $\mathcal{G}_E$  and  $\mathcal{G}_D$ , which are the encoder and decoder networks of DIG3D, respectively. Furthermore, to improve the local similarities between patches in the reconstructed image and the ground truth image, the LIPIS (Learned Perceptual Image Patch Similarity) loss [45], a perceptual similarity metric, is utilized after certain training steps. The LIPIS loss aims to optimize the perceptual quality and similarity between the reconstructed image and the ground truth image.

## 4 Experiments

### 4.1 overview

We assess the effectiveness of our method in tackling the demanding task of 3D reconstruction and novel view synthesis using a single-view RGB image. We first present the dataset and evaluation metrics employed in our study, followed by an explanation of our experimental setup. In Section 4.2, we showcase the qualitative and quantitative outcomes of novel view synthesis achieved by DIG3D, comparing it against the baseline approaches. In Section 4.3, we demonstrate the indispensability of our two-stage design and the benefits of incorporating deformable attention.

**Dataset** In our work, we utilize the widely-used ShapeNet-SRN dataset [35] for the evaluation of single-view 3D reconstruction, as introduced by [37]. This benchmark dataset comprises two object classes: "Cars" and "Chairs". The training set includes 2458 car objects and 4612 chair objects, while the validation set has 352 car objects and 662 chair objects. The testing set comprises 704 car objects and 1317 chair objects. ShapeNet-SRN provides multiple-view RGB images with corresponding camera intrinsics and poses. The dataset also includes a predefined training and testing split. For the validation and testing sets, there are 250 views per object, while the training set has 50 views per object. Each image in the dataset has a resolution of  $128 \times 128$ .

**Evaluation metrics** We train our methods using single-view RGB images and camera parameters, supervised by multiple views. During inference, we generate 3D object representations with 3D Gaussians and render novel views when provided with camera parameters. We evaluate our results using standard metrics: the Peak Signal-to-Noise Ratio (PSNR), Structural Similarity (SSIM), and perceptual quality measured using the Learned Perceptual Image Patch Similarity (LPIPS).

**Experiment Settings** Our model was trained on a single 80G A100 GPU over a period of 2 weeks, amounting to 1 million training steps. The training process followed a similar approach as presented in [37]. During the initial 800k steps, we trained the model using only the RGB loss. Subsequently, we introduced the

Table 1: Quantitative results of novel view synthesis from single view for the ShapeNet-SRN dataset.

Method	Cars			Chairs		
	PSNR $\uparrow$	SSIM $\uparrow$	LPIPS $\downarrow$	PSNR $\uparrow$	SSIM $\uparrow$	LPIPS $\downarrow$
SRN	22.25	0.88	0.129	22.89	0.89	0.104
CodeNeRF	23.80	0.91	0.128	23.66	0.90	0.166
ViewsetDiff w/o depth	23.21	0.90	0.116	24.16	0.91	0.088
PixelNeRF	23.17	0.89	0.146	23.72	0.90	0.128
VisionNeRF	22.88	0.90	0.084	24.48	0.92	0.077
NeRFDiff w/o NGD	23.95	0.92	0.092	24.80	0.93	0.070
Splatter Image	24.00	0.92	<b>0.078</b>	24.43	0.93	0.067
DIG3D	<b>24.21</b>	<b>0.92</b>	0.090	<b>24.98</b>	<b>0.94</b>	<b>0.066</b>

LPIPS loss to further enhance the training process. For the decoder architecture, we utilized 2 layers to strike a balance between performance and computational efficiency. Regarding the representation of a 3D object, we employed 10,000 Gaussians to capture its shape and properties.

## 4.2 Comparison with other methods

We compare our method with other methods on Shapenet SRN chair and car datasets in this section and analyze the performances.

**Quantitative comparison** We assess the quality of our 3D reconstruction by generating novel views of the reconstructed 3D object using the camera intrinsics and poses provided in the dataset. For each object, we calculate the average metrics for the rendered images, and the results on ShapeNet SRN are presented in Table 1. Our method surpass all the methods shown in the table for both chairs and cars.

**Visualized comparison on ShapeNet SRN** To show the quality of our method, we visualize it both for the reconstructed 3D and rendered 2D image. When it comes to rendering quality, our method surpasses Splatter Image. Our approach produces smoother and more meaningful results. For instance, in cases where one chair leg obstructs another, Splatter Image still renders the leg behind, as illustrated in Figure 4. In contrast, our method accurately captures the occlusion and generates a more realistic rendering.

To demonstrate that our method captures a meaningful 3D structure instead of merely relying on a shortcut to the supervised views, we have visualized the point cloud with the centers of Gaussians in Figure 5. In Splatter Image, each pixel in the input view is associated with a predicted depth and offset. Consequently, the network only obtains a shortcut representation of the rendered

images. When we filter out the 50% lowest opacity points, most of the background points in the input view are removed, resulting in a waste of Gaussian points. In contrast, our method ensures that all Gaussians contribute to the 3D object. The geometry of our objects is nearly accurate, and removing low opacity points does not compromise the overall 3D structure. This highlights the meaningfulness and coherence of our approach in capturing the true 3D representation of objects.

**Speed comparison** We conducted speed tests for inference on the ShapeNet SRN dataset using a single A100 GPU, and the results are summarized in Table 2.

Our method utilizing 3D Gaussian Splatting rendering technique demonstrates exceptionally fast rendering speed. Although the encoder-decoder process may take longer for the forward pass, our inference process is still fast thanks to the high rendering speed. During inference, our model performs a single forward pass to acquire the 3D Gaussian parameters and multiple passes to generate various novel views. We have the same rendering speed comparing to Splatter Image and the overall inference time remains much faster compared to PixelNeRF. The total inference time is less than 1 second.

Table 2: Inference time comparison on ShapeNet SRN Chair dataset on A100 GPU. 3D: 3d Reconstruction speed; R: rendering speed. Inference: the speed from image to all 250 novel views for each object in the test dataset. Unit in second.

Method	3D ↓	R ↓	Inference ↓
PixelNeRF	<b>0.005</b>	1.2200	304.530
Splatter Image	0.022	<b>0.0022</b>	<b>0.572</b>
DIG3D	0.140	<b>0.0022</b>	0.690

As mentioned earlier, Splatter Image takes a shortcut by focusing on views instead of accurately representing the 3D structure. This approach may yield

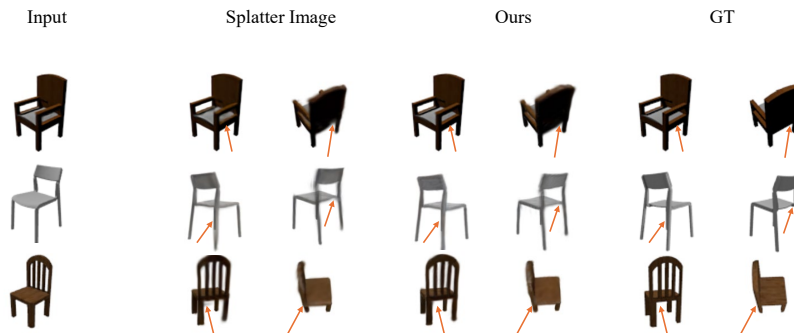


Figure 4: Novel view rendering visualization on ShapeNet SRN Chair Dataset

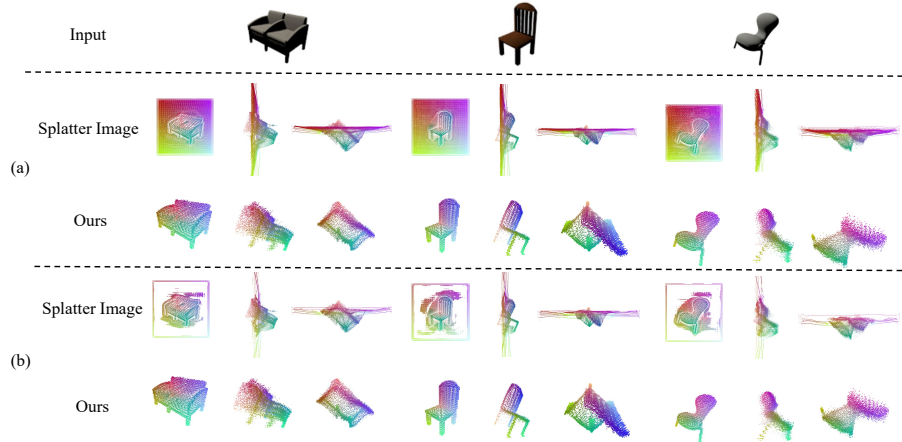


Figure 5: Point Cloud visualization. We draw the point cloud with the center of each Gaussian as a point. We show the front view, side view and top view of each point cloud. The top line of the figure shows the input view of each object. (a) shows the points without filtering. (b) shows the first 50% points with the largest opacity.

satisfactory results for views close to the input view but perform poorly for other views [22]. To support our claim, we calculate the average PSNR, SSIM, and LPIPS for each view of the ShapeNet SRN Chair dataset. As shown in Figure 6, the views within the red circle represent those that are very close to the input view. Splatter Image performance similar to our method inside the red circle but the difference is significant for the views far away. Our method demonstrates superior performance compared to Splatter Image, particularly for views that are farther away from the input view.

**Quantitative comparison view-wisely** In general, the views close to the input view will be easier to be generated because they have more information. To show the ability of generating hard situations (views far away from the input view), we present a quantitative comparison of each view in the ShapeNet SRN chair dataset, highlighting the performance of our method compared to Splatter Image. We give SSIM and LPIPS in Figure 6 in addition to PSNR in Figure 1. Our method demonstrates superior results, especially for views that are distant from the input view (index 64). These distant views pose greater challenges for novel view synthesis compared to nearby views, showcasing the robustness and generalizability of our model across various perspectives.

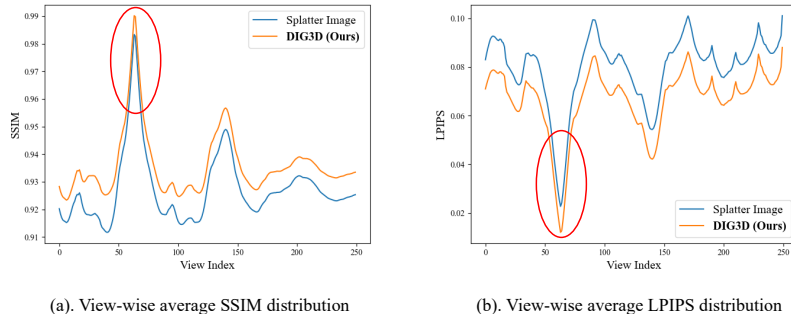


Figure 6: Comparison between our method and splatter image on PSNR, SSIM, and LPIPS for each view in ShapeNet SRN chair dataset. The input view is at index 64, the nearest views to input view are in the red circles.

#### Quantitative comparison after excluding neighbouring views

To prove that our method is not a shortcut for the input view, we conducted an experiment where we removed the views that were very close to the input view. Specifically, we excluded the nearest 8 views located within the red circle (index 60 to 68), as compared to Splatter Image. The results of this experiment, presented in Table 3, clearly indicate the superiority of our method over Splatter Image.

Table 3: Novel Views for removing the 8 nearest views to input view for ShapeNet SRN dataset

Method	Chairs		
	PSNR $\uparrow$	SSIM $\uparrow$	LPIPS $\downarrow$
Splatter Image	23.99	0.925	0.080
DIG3D	<b>24.77</b>	<b>0.935</b>	<b>0.068</b>

Our method exhibits a substantial improvement in performance compared to Splatter Image. When comparing Table 1 and Table 3, our model shows minimal decrease in metrics when removing the values of the 8 views near the input view. However, the Splatter Image dataset exhibits a notable decrement in performance. This comparison provides evidence that our method is not simply a shortcut around the input view. By removing the values of the 8 views near the input view, our method decrease not much, which highlight the effectiveness of our method in enhancing the quality of the generated views when compared to Splatter Image. These results validate that our approach performs better, particularly when it comes to generating novel views that far from input views.

### 4.3 Ablation study

To our best knowledge, DIG3D is the first one to use deformable detection transformer to 3D Gaussians. To show the significance of each component

Table 4: Ablation study on model design ShapeNet SRN Chair dataset for 100k step training

Method	Chairs		
	PSNR $\uparrow$	SSIM $\uparrow$	LPIPS $\downarrow$
w/o 3D reference point	23.300	0.9100	0.1050
w/o multi-layer refinement	21.114	0.8967	0.1328
w/o UNet feature	22.536	0.9093	0.1100
Full model	<b>23.447</b>	<b>0.9200</b>	<b>0.1000</b>

and selection of parameters of our method, we provide ablation study for each component in this section. To manage the computational cost, we trained the ablation models using a shorter training schedule of 100k iterations, following the approach of Splatter Image [37]. We discuss the trade-off of performance and efficiency for different hyperparameter selection.

**Model design** In the previous sections, we emphasized the significance of both the multi-layer refinement and 3D reference point design. Additionally, as the image extractor comprises both UNet and DinoV2, we conducted an ablation study to evaluate the impact of removing UNet.

As shown in Table 4, when the multi-layer refinement is removed, the model only receives the loss at the end of the last layer, which does not guarantee positive contributions from each layer. Without the 3D reference point, randomly selected points on the image feature may not provide sufficient accuracy in feature selection compared to the 3D Gaussian positions. Removing the UNet feature results in the image feature being solely derived from the pre-trained model, which may not be suitable for our specific task.

**Hyper-parameter selection** We give ablation study for some extremely important hyperparameters, including the number of decoder layers and the number of Gaussians utilized to represent an object in the section.

To analyze the impact of the number of Gaussians used for object representation, we conducted an ablation study. Intuitively, a higher number of Gaussians tends to enhance performance but at the cost of slower speed. Thus, we aimed to find a trade-off between model complexity and performance. The results of this study are presented in Table 5, indicating that increasing the number of Gaussians leads to improved performance. However, it is crucial to note that using an excessively large number of Gaussians significantly increases the training cost. To provide a more explicit comparison between inference time and PSNR for different numbers of Gaussians, we present Figure 7 (a). When the number of Gaussians smaller 10,000, the PSNR increases significantly. However, when the number of Gaussians exceeds 10,000, the additional benefits diminish

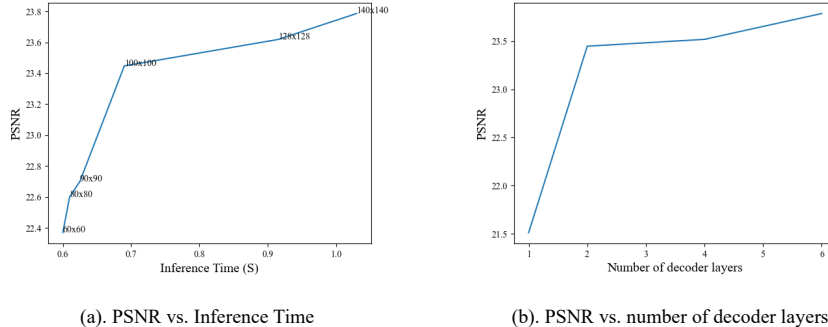


Figure 7: Ablation study for different hyperparameter selection on ShapeNet SRN chair dataset at 100k steps. (a). Inference time cost and PSNR for different number of Gaussians. We annotate the number of Gaussians at each point in the figure (e.g.  $100 \times 100$ ). (b). PSNR for different number of decoder layers.

while incurring substantial time consumption. Consequently, to strike a balance between speed and quality, we ultimately opted for 10,000 Gaussians to represent an object. This choice allows us to achieve satisfactory results while maintaining reasonable training efficiency.

Table 5: Ablation study for number of Gaussians per object on ShapeNet SRN Chair dataset for 100k step training. 3D: 3d Reconstruction speed; R: rendering speed. Test: the speed from image to all 250 novel views for each object in the test dataset.

Number of Gaussians	Chairs					
	3D (S) ↓	R (S) ↓	Test (S) ↓	PSNR ↑	SSIM ↑	LPIPS ↓
$128 \times 128$	0.24	0.0027	0.915	<b>23.453</b>	<b>0.92</b>	<b>0.11</b>
$100 \times 100$	0.14	0.0022	0.690	23.447	<b>0.92</b>	<b>0.11</b>
$80 \times 80$	0.11	0.0020	0.610	22.600	0.91	0.10

To enhance the refinement process in updating the 3D Gaussians, we employ multi-layer refinement in the decoder. In order to evaluate the influence of the number of layers in the decoder, we conducted an ablation study. The results, depicted in Table 7 (b), reveal that utilizing 2 layers yields significantly superior performance compared to using only 1 layer. Upon increasing the number of layers to 4 and 6, the observed improvement in performance is not as substantial as the transition from 1 layer to 2 layers. However, it is worth noting that the computational speed decreases significantly with the addition of more layers. Therefore, in most of our experiments, we opted to use 2 layers. Selecting 2 layers strikes a balance between performance and computational efficiency. It provides a satisfactory level of accuracy while maintaining a reasonable speed for

practical applications. However, in scenarios where higher accuracy is deemed necessary, the option to utilize more layers is available. This flexibility allows us to adapt the model’s depth to specific requirements and trade-offs between accuracy and computational resources. This finding demonstrates the importance of incorporating multiple layers in the refinement process, highlighting the effectiveness of our approach in improving the quality of the reconstructed 3D structures.

## 5 Conclusion

In conclusion, our work presents a comprehensive framework for 3D reconstruction from a single RGB image in category level. We address several limitations of previous approaches, such as incorrect geometry and shortcuts, while minimizing any negative impact on processing speed. To overcome the misalignment between input view pixels and novel view pixels, we employ separate loss functions in the encoder and decoder. Additionally, we tackle the challenge of using 2D deformable attention by introducing 3D reference points and training sampling offsets on image features, which enables efficient cross-attention calculations. We extend this approach to handle 3D queries by employing a 3D reference point strategy. This involves projecting the centers of 3D Gaussians onto image features and utilizing a multi-layer refinement strategy. Our method achieves impressive rendering speed, surpassing Splatter Image while requiring fewer Gaussians. Furthermore, we provide compelling evidence of the superiority of our method in terms of rendering quality. Our approach generates smoother and more meaningful results, accurately capturing occlusions and producing realistic renderings. We demonstrate that our method captures a meaningful 3D structure, going beyond supervised views alone. The conducted ablation studies highlight the significance of multi-layer refinement, 3D reference points, and the inclusion of UNet and pretrained DINOv2 in the image extractor.

## References

- [1] Dejan Azinović, Ricardo Martin-Brualla, Dan B Goldman, Matthias Nießner, and Justus Thies. Neural RGB-D Surface Reconstruction. In IEEE/CVF Conference on Computer Vision and Pattern Recognition (CVPR), 2022.
- [2] Jonathan T Barron, Ben Mildenhall, Matthew Tancik, Peter Hedman, Ricardo Martin-Brualla, and Pratul P Srinivasan. Mip-NeRF: A Multiscale Representation for Anti-Aliasing Neural Radiance Fields. In IEEE/CVF International Conference on Computer Vision (ICCV), 2021.
- [3] Nicolas Carion, Francisco Massa, Gabriel Synnaeve, Nicolas Usunier, Alexander Kirillov, and Sergey Zagoruyko. End-to-end object detection with transformers. In European conference on computer vision (ECCV), 2020.

- [4] Guikun Chen and Wenguan Wang. A Survey on 3D Gaussian Splatting. ArXiv, 2024.
- [5] Yiwen Chen, Zilong Chen, Chi Zhang, Feng Wang, Xiaofeng Yang, Yikai Wang, Zhongang Cai, Lei Yang, Huaping Liu, and Guosheng Lin. GaussianEditor: Swift and Controllable 3D Editing with Gaussian Splatting. In IEEE/CVF Conference on Computer Vision and Pattern Recognition (CVPR), 2024.
- [6] Christopher Bongsoo Choy, Danfei Xu, JunYoung Gwak, Kevin Chen, and Silvio Savarese. 3D-R2N2: A Unified Approach for Single and Multi-view 3D Object Reconstruction. In European conference on computer vision (ECCV), 2016.
- [7] Haoqiang Fan, Hao Su, and Leonidas J. Guibas. A Point Set Generation Network for 3D Object Reconstruction from a Single Image. In IEEE/CVF Conference on Computer Vision and Pattern Recognition (CVPR), 2016.
- [8] Sara Fridovich-Keil, Alex Yu, Matthew Tancik, Qinhong Chen, Benjamin Recht, and Angjoo Kanazawa. Plenoxels: Radiance fields without neural networks. In IEEE/CVF Conference on Computer Vision and Pattern Recognition (CVPR), 2022.
- [9] Stephan J. Garbin, Marek Kowalski, Matthew Johnson, Jamie Shotton, and Julien P. C. Valentin. FastNeRF: High-Fidelity Neural Rendering at 200FPS. In IEEE/CVF International Conference on Computer Vision (ICCV), 2021.
- [10] Jiatao Gu, Alex Trevithick, Kai-En Lin, Joshua M. Susskind, Christian Theobalt, Lingjie Liu, and Ravi Ramamoorthi. NerfDiff: Single-image View Synthesis with NeRF-guided Distillation from 3D-aware Diffusion. In International Conference on Machine Learning (ICML), 2023.
- [11] Peter Hedman, Pratul P. Srinivasan, Ben Mildenhall, Jonathan T. Barron, and Paul E. Debevec. Baking Neural Radiance Fields for Real-Time View Synthesis. In IEEE/CVF International Conference on Computer Vision (ICCV), 2021.
- [12] Wonbong Jang and Lourdes Agapito. CodeNeRF: Disentangled Neural Radiance Fields for Object Categories. In IEEE/CVF Conference on Computer Vision and Pattern Recognition (CVPR), 2021.
- [13] Bernhard Kerbl, Georgios Kopanas, Thomas Leimkuehler, and George Drettakis. 3D Gaussian Splatting for Real-Time Radiance Field Rendering. In ACM Transactions on Graphics (TOG), 2023.
- [14] Feng Li, Hao Zhang, Shilong Liu, Jian Guo, Lionel M Ni, and Lei Zhang. DN-DETR: Accelerate DETR Training by Introducing Query DeNoising. In IEEE/CVF Conference on Computer Vision and Pattern Recognition (CVPR), 2022.

- [15] Feng Li, Ailing Zeng, Siyi Liu, Hao Zhang, Hongyang Li, Lei Zhang, and Lionel Ming shuan Ni. Lite DETR : An Interleaved Multi-Scale Encoder for Efficient DETR. In IEEE/CVF Conference on Computer Vision and Pattern Recognition (CVPR), 2023.
- [16] Feng Li, Hao Zhang, Hu-Sheng Xu, Siyi Liu, Lei Zhang, Lionel Ming shuan Ni, and Heung yeung Shum. Mask DINO: Towards A Unified Transformer-based Framework for Object Detection and Segmentation. In IEEE/CVF Conference on Computer Vision and Pattern Recognition (CVPR), 2023.
- [17] Hongyang Li, Hao Zhang, Shilong Liu, Zhaoyang Zeng, Tianhe Ren, Feng Li, and Lei Zhang. TAPTR: Tracking Any Point with Transformers as Detection. ArXiv, 2024.
- [18] Ruilong Li, Hang Gao, Matthew Tancik, and Angjoo Kanazawa. NerfAcc: Efficient Sampling Accelerates NeRFs. In IEEE/CVF International Conference on Computer Vision (ICCV), 2023.
- [19] Sicheng Li, Hao Li, Yue Wang, Yiyi Liao, and Lu Yu. SteerNeRF: Accelerating NeRF Rendering via Smooth Viewpoint Trajectory. In IEEE/CVF Conference on Computer Vision and Pattern Recognition (CVPR), 2023.
- [20] Kai-En Lin, Yen-Chen Lin, Wei-Sheng Lai, Tsung-Yi Lin, Yichang Shih, and Ravi Ramamoorthi. Vision Transformer for NeRF-Based View Synthesis from a Single Input Image. In 2023 IEEE/CVF Winter Conference on Applications of Computer Vision (WACV), 2022.
- [21] Tsung-Yi Lin, Piotr Dollár, Ross B. Girshick, Kaiming He, Bharath Hariharan, and Serge J. Belongie. Feature Pyramid Networks for Object Detection. In IEEE/CVF Conference on Computer Vision and Pattern Recognition (CVPR), 2017.
- [22] Kenkun Liu, Derong Jin, Ailing Zeng, Xiaoguang Han, and Lei Zhang. A Comprehensive Benchmark for Neural Human Radiance Fields. In Conference on Neural Information Processing Systems (NIPS), 2024.
- [23] Minghua Liu, Chao Xu, Haiyan Jin, Linghao Chen, Mukund Varma T, Zexiang Xu, and Hao Su. One-2-3-45: Any single image to 3d mesh in 45 seconds without per-shape optimization. In Conference on Neural Information Processing Systems (NIPS), 2024.
- [24] Ruoshi Liu, Rundi Wu, Basile Van Hoorick, Pavel Tokmakov, Sergey Zakharov, and Carl Vondrick. Zero-1-to-3: Zero-shot One Image to 3D Object. In IEEE/CVF International Conference on Computer Vision (ICCV), 2023.
- [25] Shilong Liu, Feng Li, Hao Zhang, Xiao Yang, Xianbiao Qi, Hang Su, Jun Zhu, and Lei Zhang. DAB-DETR: Dynamic anchor boxes are better queries for DETR. In International Conference on Learning Representations (ICLR), 2022.

- [26] Shilong Liu, Zhaoyang Zeng, Tianhe Ren, Feng Li, Hao Zhang, Jie Yang, Chun yue Li, Jianwei Yang, Hang Su, Jun-Juan Zhu, and Lei Zhang. Grounding DINO: Marrying DINO with Grounded Pre-Training for Open-Set Object Detection. ArXiv, 2023.
- [27] Siyi Liu, Tianhe Ren, Jia-Yu Chen, Zhaoyang Zeng, Hao Zhang, Feng Li, Hongyang Li, Jun Huang, Hang Su, Jun-Juan Zhu, and Lei Zhang. Stable-DINO: Detection Transformer with Stable Matching. In IEEE/CVF International Conference on Computer Vision (ICCV), 2023.
- [28] Xiaoyang Lyu, Yang-Tian Sun, Yi-Hua Huang, Xiuzhe Wu, Ziyi Yang, Yilun Chen, Jiangmiao Pang, and Xiaojuan Qi. 3DGSR: Implicit Surface Reconstruction with 3D Gaussian Splatting. ArXiv, 2024.
- [29] Ben Mildenhall, Pratul P. Srinivasan, Matthew Tancik, Jonathan T. Barron, Ravi Ramamoorthi, and Ren Ng. NeRF: Representing Scenes as Neural Radiance Fields for View Synthesis. In The European Conference on Computer Vision (ECCV), 2020.
- [30] Thomas Müller, Alex Evans, Christoph Schied, and Alexander Keller. Instant Neural Graphics Primitives with a Multiresolution Hash Encoding. In ACM Transactions on Graphics (SIGGRAPH), 2022.
- [31] Maxime Oquab, Timothée Darcet, Théo Moutakanni, Huy Q. Vo, Marc Szafraniec, Vasil Khalidov, Pierre Fernandez, Daniel Haziza, Francisco Massa, Alaaeldin El-Nouby, Mahmoud Assran, Nicolas Ballas, Wojciech Galuba, Russ Howes, Po-Yao (Bernie) Huang, Shang-Wen Li, Ishan Misra, Michael G. Rabbat, Vasu Sharma, Gabriel Synnaeve, Huijiao Xu, Hervé Jégou, Julien Mairal, Patrick Labatut, Armand Joulin, and Piotr Bojanowski. DINOv2: Learning Robust Visual Features without Supervision. In Transactions on Machine Learning Research (TMLR), 2024.
- [32] Marie-Julie Rakotosaona, Fabian Manhardt, Diego Martin Arroyo, Michael Niemeyer, Abhijit Kundu, and Federico Tombari. NeRFMeshing: Distilling Neural Radiance Fields into Geometrically-Accurate 3D Meshes. In International Conference on 3D Vision (3DV), 2023.
- [33] Tianhe Ren, Siyi Liu, Feng Li, Hao Zhang, Ailing Zeng, Jie Yang, Xingyu Liao, Ding Jia, Hongyang Li, He Cao, Jianan Wang, Zhaoyang Zeng, Xianbiao Qi, Yuhui Yuan, Jianwei Yang, and Lei Zhang. detrex: Benchmarking Detection Transformers. ArXiv, 2023.
- [34] Olaf Ronneberger, Philipp Fischer, and Thomas Brox. U-net: Convolutional networks for biomedical image segmentation. In Medical image computing and computer-assisted intervention (MICCAI), 2015.
- [35] Vincent Sitzmann, Michael Zollhoefer, and Gordon Wetzstein. Scene Representation Networks: Continuous 3D-Structure-Aware Neural Scene Representations. In Conference on Neural Information Processing Systems (NIPS), 2019.

- [36] Jiaming Song, Chenlin Meng, and Stefano Ermon. Denoising Diffusion Implicit Models. In International Conference on Learning Representations (ICLR), 2021.
- [37] Stanislaw Szymanowicz, Christian Rupprecht, and Andrea Vedaldi. Splat-ter Image: Ultra-Fast Single-View 3D Reconstruction. In IEEE/CVF Conference on Computer Vision and Pattern Recognition (CVPR), 2024.
- [38] Jiaxiang Tang, Jiawei Ren, Hang Zhou, Ziwei Liu, and Gang Zeng. Dream-Gaussian: Generative Gaussian Splatting for Efficient 3D Content Creation. In International Conference on Learning Representations (ICLR), 2024.
- [39] Dor Verbin, Peter Hedman, Ben Mildenhall, Todd E. Zickler, Jonathan T. Barron, and Pratul P. Srinivasan. Ref-NeRF: Structured View-Dependent Appearance for Neural Radiance Fields. In IEEE/CVF Conference on Computer Vision and Pattern Recognition (CVPR), 2022.
- [40] Yaniv Wolf, Amit Bracha, and Ron Kimmel. Surface Reconstruction from Gaussian Splatting via Novel Stereo Views. ArXiv, 2024.
- [41] Lior Yariv, Jiatao Gu, Yoni Kasten, and Yaron Lipman. Volume rendering of neural implicit surfaces. In Conference on Neural Information Processing Systems (NIPS), 2021.
- [42] Alex Yu, Vickie Ye, Matthew Tancik, and Angjoo Kanazawa. pixelNeRF: Neural Radiance Fields from One or Few Images. In IEEE/CVF Conference on Computer Vision and Pattern Recognition (CVPR), 2021.
- [43] Hao Zhang, Feng Li, Shilong Liu, Lei Zhang, Hang Su, Jun-Juan Zhu, Lionel Ming shuan Ni, and Heung yeung Shum. DINO: DETR with Improved DeNoising Anchor Boxes for End-to-End Object Detection. In The International Conference on Learning Representations (ICLR), 2023.
- [44] Kai Zhang, Gernot Riegler, Noah Snavely, and Vladlen Koltun. NeRF++: Analyzing and Improving Neural Radiance Fields. ArXiv, 2020.
- [45] Richard Zhang, Phillip Isola, Alexei A. Efros, Eli Shechtman, and Oliver Wang. The Unreasonable Effectiveness of Deep Features as a Perceptual Metric. In IEEE/CVF Conference on Computer Vision and Pattern Recognition (CVPR), 2018.
- [46] Xizhou Zhu, Weijie Su, Lewei Lu, Bin Li, Xiaogang Wang, and Jifeng Dai. Deformable DETR: Deformable Transformers for End-to-End Object Detection. In The International Conference on Learning Representations (ICLR), 2021.
- [47] M. Zwicker, H. Pfister, J. van Baar, and M. Gross. EWA volume splatting. In IEEE Visualization (IEEE VIS), 2001.